Research Article | Vol. 32, No. 17 / 12 Aug 2024 / Optics Express 30824
Optics EXPRESS

Sub-cycle dynamics in two-color high-harmonic generation from laser-produced plasmas

JAN MATHIJSSEN,[1,2] EDCEL J. SALUMBIDES,[1,2] KJELD S. E. EIKEMA,[1,2] AND STEFAN WITTE[1,2,*]

[1]Advanced Research Center for Nanolithography, Science Park 106, 1098 XG Amsterdam, The Netherlands
[2]Vrije Universiteit Amsterdam, De Boelelaan 1105, 1081 HV, Amsterdam, The Netherlands
[*]witte@arcnl.nl

Abstract: We present high-order harmonic generation (HHG) in laser-produced aluminium and tin plasmas driven by a two-color field with orthogonal polarization, leading to the generation of both odd and even harmonics. We shape the effective drive field with sub-cycle resolution by controlling the phase between the fundamental wave and its second harmonic. The shape of the drive field influences the electron trajectories of the various harmonics generated in these plasmas. Here we focus on intermediate harmonic orders, with energies around the ionization potential of the target atoms. Clear oscillatory signals are observed in the HHG signals, with strongly harmonic-order-dependent modulation depth and oscillation phase. These results provide evidence for a significant influence of the Coulomb potential on the laser-driven electron trajectories in this spectral range.

1. Introduction: high-harmonic generation in laser-produced plasmas

High-order harmonic generation (HHG) is an effective method to generate coherent radiation in the extreme-ultraviolet (XUV) and soft-X-ray spectral ranges with a compact table-top setup (see e.g. [1,2]). In HHG, an intense ultrashort laser pulse nonlinearly interacts with a medium, leading to the generation of new spectral components that typically appear as high-order harmonics of the driving laser frequency. While low-order harmonic generation [3,4] was discovered and understood shortly after the invention of the laser, the observation of higher-order harmonics required a non-perturbative theory to be developed. This led to the concept of the three-step model [5,6], in which electrons tunnel ionize from a ground-state atom, accelerate in the laser field, and recombine with the parent ion, leading to emission of a high-energy photon. The recurring nature of the process at every fundamental field half-cycle results in a train of attosecond light bursts [7], and the time-integrated spectrum consists of discrete harmonics.

Although the most basic version of the three-step model only considers an ionization potential, it was shown that atomic structure can have a significant impact on HHG spectra. The presence of atomic transitions near harmonic frequencies can result in strong resonance enhancement of specific harmonics [8–10], as well as absorption and spectral reshaping [11,12]. Thus, the use of specific atomic species can have advantages for the generation of controlled XUV spectra, such as in producing quasi-monochromatic beams. While most HHG experiments employ inert gas-phase elements such as noble gases because of their high ionization potential, favourable transparency and ease-of-use, resonance-induced effects are more readily found in other elements such as metals. Such metallic elements then need to be converted to the gas phase at sufficient pressure to enable HHG, typically via laser-driven vaporization with an auxiliary pump pulse [11]. The resulting laser-produced plasma (LPP) can be used for HHG, while the pump laser parameters may provide an additional level of control [13].

For a single-wavelength laser field in an isotropic medium, the waveform of the subsequent generated light bursts at each half cycle is very similar, except for a π phase shift, causing only odd-order harmonics to be produced. By introducing an asymmetry between positive and negative

#531520 https://doi.org/10.1364/OE.531520
Journal © 2024 Received 29 May 2024; revised 18 Jul 2024; accepted 19 Jul 2024; published 9 Aug 2024

Optics EXPRESS

half-cycles of the electric field, even-order harmonics can be generated as well. Experimentally such an asymmetry can be realized in anisotropic media, or optically by the addition of a laser field at twice the fundamental frequency [14,15]. The addition of a second-harmonic (2ω) field therefore enables more harmonics to be produced in isotropic media. This option has been explored for LPP-based HHG, leading to the generation of even-order harmonics [16], resonance enhancement of these harmonics [17], as well as modified phase matching properties as a function of the two-color field parameters [18–20].

An interesting insight from Dudovich et al. was that such a 2ω field can actually be used as a temporal gate that selects specific harmonics [21]. Especially if the 2ω field is polarized perpendicularly to the fundamental field, it can control the recombination step in a time-dependent way [22], thus selecting electron trajectories with specific energies as a function of the relative phase between the ω and 2ω fields. The interpretation of this attosecond gating mechanism is usually given in terms of the three-step model, where a weak 2ω field is expected to modulate the recombination step by spatially offsetting the electron with respect to the parent ion at the time of recombination [21]. This picture is found to work well for high-order harmonics in the plateau region, but in its basic form does not take the Coulomb potential of the atom or any other atomic structure into account. Extensions to the theory that include Coulomb effects have also been developed [23–25], leading to even better agreement with experimental determinations of the time delays and associated phase shifts on the harmonics. For lower-order harmonics however, such an interpretation can become questionable, as a classical electron trajectory at such low energies remains so close to the parent ion that the atomic potential should have a significant influence. The strong-field theory, also including Coulomb correction, calculates the action of the free electron in the continuum, which is not well defined for electron energies below the ionization potential. Therefore, application of such strong-field models to the presently studied HHG parameter range will lead to challenges. Two-color gating typically shows only weak phase dependence for plateau harmonics [15,21], with an increasing effect towards the HHG cutoff energy where the electron trajectories qualitatively change [26].

In this paper, we present experimental results on a two-color HHG experiment in LPPs from aluminium (Al) and tin (Sn), in which we focus on the lower-order harmonics. We record HHG spectra as a function of the relative phase between perpendicularly polarized ω and 2ω fields. We observe significant oscillations particularly at the even-order harmonic frequencies, with significant variations in the relative phase of those oscillations between subsequent harmonics. Our results provide evidence that the sub-cycle electron dynamics at these harmonic frequencies are indeed significantly influenced by the atomic potential.

2. Theory: HHG in perpendicularly polarized two-color fields

As mentioned, a theoretical description of the HHG process is usually based on the three-step model [5,6], which has been well established for harmonics with energies well above the ionization potential. However, at lower energies the influence of the atomic potential can be expected to have a significant influence on the electron trajectory, complicating such a model description. Therefore, we take a more phenomenological approach to describe the influence of the perpendicularly polarized two-color field on the HHG emission, based on the model introduced by He et al. [26] for parallel fields.

As a starting point, we assume that in a single-color field the HHG radiation is emitted in the form of short XUV bursts twice per IR cycle, over n cycles of the laser field (Fig. 1(a)). This results in the well known HHG spectrum with discrete odd harmonics spaced by 2ω (Fig. 1(c)). Adding a 2ω field with its polarization parallel to the ω field introduces an asymmetry in the combined field, leading to different amplitudes and phases for the XUV bursts of the first and second half cycles (Fig. 1(b)). Consequently, even harmonics (purple peaks in Fig. 1(d)) appear in the HHG spectrum. Extending this concept to two dimensions for orthogonally-polarized ω

Optics EXPRESS

(polarized along $\hat{x}$) and 2ω (polarized along $\hat{y}$) driving fields, the XUV pulse trains in the $\hat{x}$ and $\hat{y}$ directions can be formulated as:

$$S_x(t) = \sum_{j=1}^{n} a_+(t) \otimes \delta(t - jT) + a_-(t) \otimes \delta(t - jT - \frac{T}{2})\hat{x}, \quad (1)$$

$$S_y(t) = \sum_{j=1}^{n} b_+(t) \otimes \delta(t - jT) + b_-(t) \otimes \delta(t - jT - \frac{T}{2})\hat{y}. \quad (2)$$

Here $a_+(t), b_+(t), a_-(t)$, and $b_-(t)$ are the XUV bursts emitted in the first and second half IR cycles, and T is the period of the fundamental field. The magnitudes of $a_\pm(t)$ and $b_\pm(t)$ depend on the trajectory that the electron takes in the laser field. To understand the dependence of $a_\pm(t)$ and $b_\pm(t)$ on the relative phase φ between the two laser fields, it is instructive to visualize the electron motion in such a two-color field in the vicinity of an atom. Figures 2(a,c) show such trajectories for consecutive half-cycles of the fundamental field for a given phase φ between the two fields, in an atom with a p-wave ground state. Figures 2(c,d) show such trajectories for a different phase φ. From these trajectories, the relative signs of $a_\pm(t)$ and $b_\pm(t)$ can be inferred.

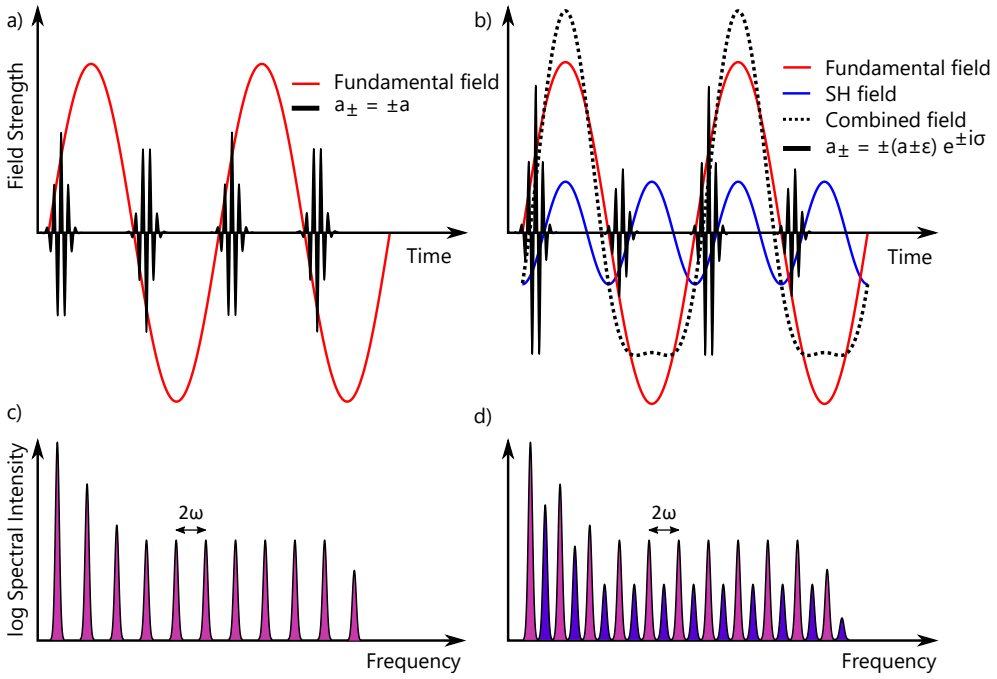

Fig. 1. Schematic representation of XUV bursts generated by the HHG process. a) and b), time domain illustration for HHG ω and 2ω driving fields with a relative phase of $\pi/2$, respectively. The red curve shows the fundamental field, the blue curve represents its second harmonic and the black-dotted line shows the combined HHG driving field. Solid black pulses represent the $a_\pm$ XUV bursts. c,d), schematic drawings of resulting spectral HHG intensities driven by ω and 2ω fields, respectively. Odd harmonics are colored pink and even harmonics are colored purple.

For a p-wave atomic wave function, initial electron motion and ionization preferentially occur parallel to the p-wave axis [27], which acts as a selection mechanism for atoms with a specific orbital alignment (which remains valid for atomic orbitals with different quantum numbers).

Optics EXPRESS

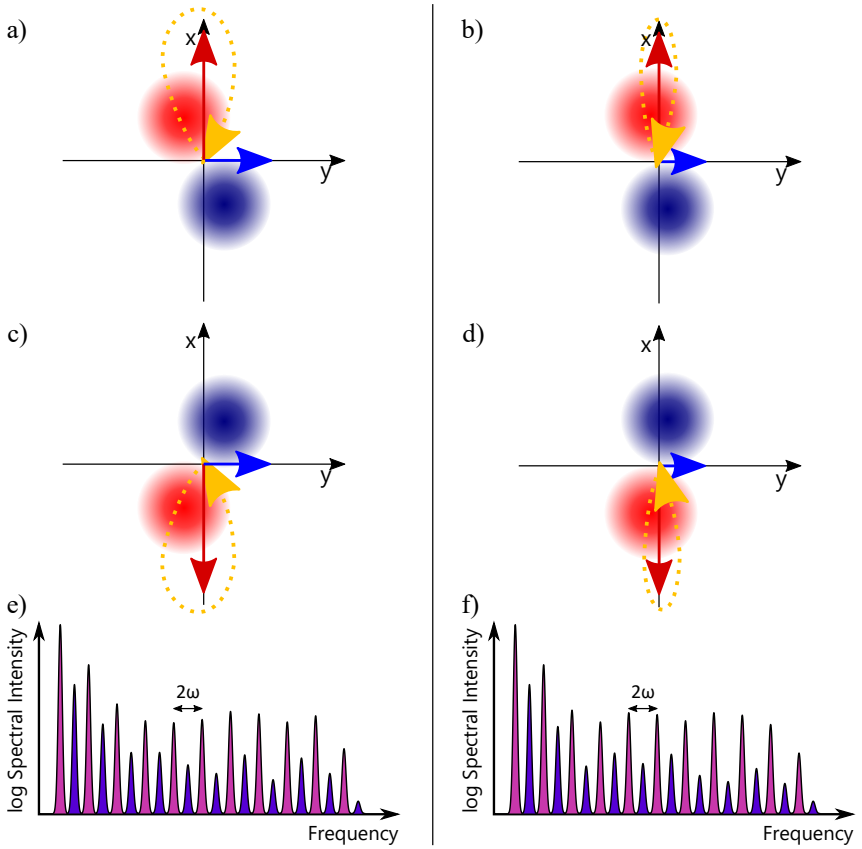

Fig. 2. Schematic drawing of electron trajectories (orange paths) in a two-color field with perpendicular polarizations. The fundamental and second harmonic are indicated by red and blue vectors, respectively. a) Schematic trajectory for a given phase between the fields, in an atom with a p-orbital ground state. The initial motion is preferentially along the orbital axis (see text and [27]). b) Schematic electron trajectory for another relative phase between the fields. The motion through the atomic potential is different compared to the trajectory in a. c) Trajectory in the next half-cycle for the fields similar to a. d) Trajectory in the next half-cycle for the fields similar to b. e,f) Schematic drawings of the resulting HHG spectra. The relative intensities of the harmonics depend on the phase between the fields.

The electron motion in the two-color field then results in a non-zero return angle with respect to the orbital, where the angle is influenced by φ. In the strong-field approximation, this can be interpreted as control over the recollision angle, and used for atomic state tomography [22]. More generally, even for lower electron energies the emitted harmonics can be seen as resulting from the interference of the returning electron wave with the ground state, described by a dipole matrix element $\mathbf{d} = \langle\psi_g|\mathbf{r}|\psi_{el}\rangle$. The magnitude of this dipole at a given frequency determines the strength of the generated field, and the emission direction is perpendicular to the dipole. The projections of this dipole along the polarization directions of the fundamental and second-harmonic fields then give $a(t)$ and $b(t)$: $a(t) = \mathbf{d}\sin\theta$ and $b(t) = \mathbf{d}\cos\theta$, with θ the angle between the dipole and the fundamental polarization direction (the x-axis in Fig. 2). In a non-centrosymmetric atomic potential, the two-color field leads to a complex electron trajectory and in general a nonzero return angle with respect to the ground-state orbital, influencing $\mathbf{d}$ and making it dependent on the phase φ. The mirror symmetry (neglecting carrier envelope phase

Optics EXPRESS

changes and ionization effects) between consecutive half-cycles (compare Figs. 2(a,c)) ensures that $a_+(t) = -a_-(t) = \pm a(t,\varphi)$ and $b_+(t) = b_-(t) = b(t,\varphi)$, where in the latter case no sign change takes place because the driving field in the y-direction is the second harmonic.

With this conceptual understanding of the generation mechanism, a description of the resulting harmonic fields in the spectral domain can be obtained by Fourier transforming Eqs. (1) and (2), resulting in:

$$S_x(\Omega,\varphi) = \hat{x}A(\Omega,\varphi)\sum_{j=1}^{n} e^{ij\Omega T} - e^{ij\Omega T + i\frac{\Omega T}{2}}, \tag{3}$$

$$S_y(\Omega,\varphi) = \hat{y}B(\Omega,\varphi)\sum_{j=1}^{n} e^{ij\Omega T} + e^{ij\Omega T + i\frac{\Omega T}{2}}, \tag{4}$$

where $A(\Omega,\varphi)$ and $B(\Omega,\varphi)$ are the Fourier transforms of $a(t,\varphi)$ and $b(t,\varphi)$. The resulting spectral intensity of the HHG radiation in the $\hat{x}$ and $\hat{y}$ directions can then finally be expressed as:

$$|S_x(\Omega,\varphi)|^2 = 4|A(\Omega,\varphi)|^2 \cdot \left|\frac{\sin(\frac{n\Omega T}{2})}{\sin(\frac{\Omega T}{2})}\right|^2 \cdot \sin^2(\frac{\Omega T}{4}), \tag{5}$$

$$|S_y(\Omega,\varphi)|^2 = 4|B(\Omega,\varphi)|^2 \cdot \left|\frac{\sin(\frac{n\Omega T}{2})}{\sin(\frac{\Omega T}{2})}\right|^2 \cdot \cos^2(\frac{\Omega T}{4}). \tag{6}$$

The $A|(\Omega,\varphi)|^2$ and $|B(\Omega,\varphi)|^2$ terms in these equations describe the spectral intensity of the emitted harmonics at frequencies $\Omega = q\omega$. The second term represents a comb of both odd and even q harmonics. As the number of laser cycles n increases, the width of the comb peaks decreases, reflecting the temporal coherence properties of the pulse train. The last term acts as a modulation on the harmonic spectrum, which has the effect of cancelling the even harmonics in $|S_x|^2$ and the odd harmonics in $|S_y|^2$. Thus, the odd harmonics are polarized in the direction of the fundamental beam and the even harmonics are polarized along the direction of the second harmonic. Given the dependence of $|S_x|^2$ and $|S_y|^2$ on the phase φ between the fundamental and second-harmonic fields, we can expect intensity modulations of the harmonics with a period corresponding to half of a second-harmonic field cycle. The relative intensity of the second harmonic pulses in the current experiment is limited to 1% of the fundamental pulse energy. Hence, we expect the second harmonic field to act as a perturbation to the fundamental field, resulting in a spectrum with strong odd and weak even harmonics. Furthermore, in our HHG spectrometer (see next section) we cannot determine the polarization state of the harmonics. The relative phase φ between the fundamental and second-harmonic fields is controlled by changing the difference in optical path length $\Delta\Lambda$ for the two wavelengths, which in our experiment are 1560 nm for the fundamental and 780 nm for the second harmonic. A phase shift of 2π therefore corresponds to a difference in path length of 390 nm, i.e. $\varphi/2\pi = \Delta\Lambda/390\,nm$. We then expect to observe harmonics that vary in intensity according to the following relation:

$$I_H(\Delta\Lambda) = A_H \cdot \sin^2\left(\frac{\pi\Delta\Lambda}{390\,nm} + \frac{\phi_H}{2}\right) + O_H. \tag{7}$$

Here, A_H is the modulation depth of harmonic H, ϕ_H is its phase offset, and O_H is the intensity offset. In this equation, we have set the oscillation period to correspond with an optical path length difference $\Delta\Lambda$ of half the second-harmonic wavelength.

For plateau harmonics well above the ionization potential, which are well described by the strong-field approximation, such modulations are only weakly dependent on harmonic number [21,26]. In the lower-energy regime considered here, it can be expected that the atomic potential will have a significant influence on the electron motion at different energies. Therefore, the optimum intensity of each harmonic may vary more strongly with phase φ.

Optics EXPRESS

3. Experimental setup for plasma-based two-color HHG

A schematic overview of the experimental setup is shown in Fig. 3. The vacuum system consists of a target chamber where the HHG process takes place, and an EUV spectrometer. A target for plasma generation and HHG is positioned in the experimental chamber. Pump pulses with a duration of 0.43 ns and an energy up to 4 mJ are sent onto this target under normal incidence, creating an expanding LPP. After a certain delay, pulses from the fundamental beam (central wavelength = 1560 nm, energy = 0.5 mJ, pulsewidth = 200 fs) are then sent through this LPP in a direction parallel to the target surface, generating the high-order harmonics within the plasma. The intensity at the focus is estimated to be 0.8×10^{14} W/cm^2. The toroidal mirror in the spectrometer images the HHG spot onto an EUV-sensitive camera. The HHG radiation is spectrally dispersed with a transmission grating with a groove density of 1000 mm^{-1}, after which the 1st diffraction order is resolved on the EUV camera. The grating also acts as an aperture to the HHG beam, blocking parts of the beam with higher divergence such as long trajectories for above-threshold harmonics. The 0th and -1^{st} orders are blocked with a beam dump to prevent scattered signal and damage of the EUV camera. The laser systems used to generate the pump and HHG pulses have been described in detail previously [28,29].

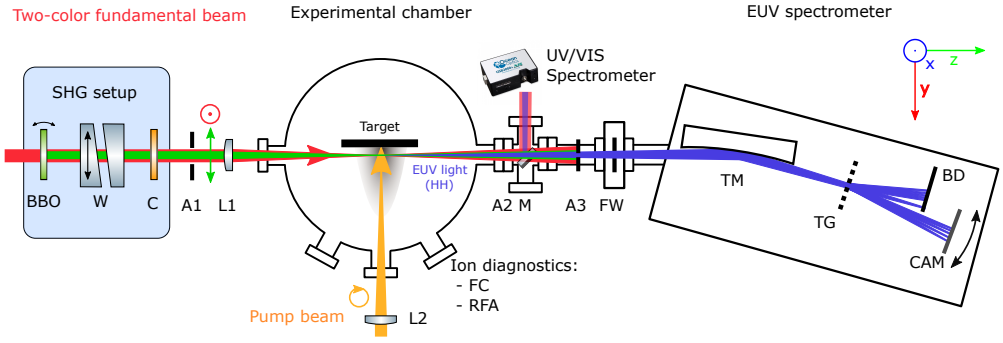

Fig. 3. Schematic image of the experimental setup. At the bottom and left side, the pump laser and the HHG driving laser with the SHG setup are depicted, respectively. The right side of the schematic shows the experimental chamber in which the high harmonics are generated and the EUV spectrometer. Laser parameters for these experiments were set as follows: pump pulse length: 0.43 ns, pump pulse energy = 2 mJ, fundamental pulse length = 200 fs, fundamental pulse energy = 0.5 mJ, second harmonic energy up to 5 µJ, polarization states are indicated with the respective arrows. Optical components: BBO: nonlinear crystal for frequency doubling, W: UV fused silica wedges, C: calcite plate, A: Aperture, L1: f = 300 mm lens, L2: f = 1000 mm lens, M: insertable mirror, FW: filter wheel, FC: Faraday cup, RFA: retarding field energy analyser, TM: toroidal mirror, TG: transmission grating, BD: beam dump, CAM: EUV camera.

A second-harmonic generation (SHG) stage has been implemented in front of the target chamber, enabling phase-controlled two-color HHG experiments [15,21,22,30]. The SHG stage contains a 200 μm thick type-I BBO crystal cut at $\theta = 19.8°$. The ratio between SHG and fundamental energy can be tuned via the phase matching angle. The relative phase between the fundamental and second harmonic is controlled with a pair of fused silica wedges. Varying the inserted amount of glass results in a wavelength-dependent path length difference $\Delta\Lambda = \Delta n \Delta x \tan\Phi$, where Δx is the transverse wedge displacement and $\Phi = 5°$ is the apex angle of the wedge pair. For UV fused silica, the refractive index difference between the fundamental and its second harmonic $\Delta n = n_{1560} - n_{780} = -0.0098$ [31]. This results in a path length difference of $\Delta\Lambda = 857$ nm per millimeter wedge displacement. A delay of half a second-harmonic cycle – which is the expected periodicity of the oscillations – is thus achieved by shifting the wedge by 455 µm.

Optics EXPRESS

Accurate path length variation is performed by mounting one of the wedges on a high-accuracy linear piezo-stage (Smaract, model number SLC1760). As the focusing lens and the vacuum viewport also add a time delay due to their group-delay mismatch between fundamental and second harmonic, some additional group-delay compensation is needed to maximize temporal overlap at the plasma. This compensation is achieved with a 1.7 mm thick calcite plate, cut at an angle of $\Theta = 55°$, inserted in the two-color beam. Initial alignment optimization was done by maximizing the sum-frequency generation signal of the two colors produced in another BBO crystal, positioned behind all optical components of the beamline to best mimic experimental conditions. However, as the driving pulses for this experiment are on the long side, the optimum phase matching for the HHG process likely occurs mainly in the leading edge of the fundamental pulse. Therefore, final optimization of the temporal overlap is done by maximizing the signal of the even harmonics measured under typical experimental conditions.

The pump pulse energy for the Al targets was set at 4 mJ while Sn targets were irradiated by pump pulses with energies of 2 mJ, since those parameters lead to the highest signal yield for these materials. The focal spot size of the pump laser on the target is measured to be 450 μm (e^{-2} diameter). The delay between the pump and fundamental pulses has been set to 100 ns. The fundamental pulse length was measured to be 200 fs. Its energy has been limited to 0.5 mJ, to reduce noise originating from stray light of the second harmonic on the EUV camera, as the Si chip of this camera is highly sensitive to this wavelength. To further suppress this stray light, a polarization scheme with vertically polarized fundamental and horizontally polarized second harmonic has been utilized to reduce the second harmonic reflection efficiency of the toroidal mirror. An unfortunate consequence of this polarization setting is that the even harmonics generated in the experimental chamber also experience a sub-optimal reflection on the toroidal mirror, resulting in an underestimation of the intensity ratio of even and odd harmonics. Based on the optical properties of the boron carbide coating on the toroidal mirror, the strength of the 6^{th} harmonic (H6) is likely underestimated by a factor four, while H12 is likely underestimated up to a factor two. We do not compensate for these effects in the data processing, and present the measured harmonic yield after only static background correction.

For the experiments on Sn, we have scanned the wedge position over 630 μm, corresponding to 0.69 optical cycles of the second harmonic. These measurements were carried out with 5 μJ second harmonic energy, corresponding to a 1% intensity ratio between fundamental and second harmonic. For the Al experiments, we have performed measurements at SHG energies of 0.5 μJ, 2.0 μJ and 5.0 μJ. At the highest energy, we carried out a longer phase scan covering nearly 1.4 optical cycles of the second harmonic.

4. Results: phase-dependence in two-color HHG

4.1. Typical harmonic spectra for Al and Sn

Typical HHG spectra measured in Al and Sn plasmas are shown in Figs. 4 and 5, respectively. Both spectra are acquired under identical HHG driving conditions ($E_\omega = 0.5$ mJ, $E_{2\omega} = 5$ μJ, 100 ns delay between pump and fundamental). The aluminium and tin targets are pumped with 4 mJ and 2 mJ, as aluminium targets require more energy to ablate. The spectrometer is set to cover a wavelength range between 115 nm and 295 nm. Harmonics 6 up to 13 are contained within this spectral region. The corresponding peaks are marked in the plotted spectra. The additional peaks appearing at wavelengths 210 nm, 240 nm and 285 nm result from second order diffraction of harmonics 15, 13 and 11, respectively.

To assess the harmonic yield, the detected signal is averaged over a region of interest (ROI) around each harmonic peak, indicated by the red rectangles in Figs. 4 and 5. Note that due to a small rotation of the transmission grating, harmonic 6 in the aluminium spectrum is off-center with respect to the selected ROI, underestimating its strength slightly. This does not influence the detection of oscillatory signals as discussed later, although the signal to noise ratio is somewhat

Optics EXPRESS

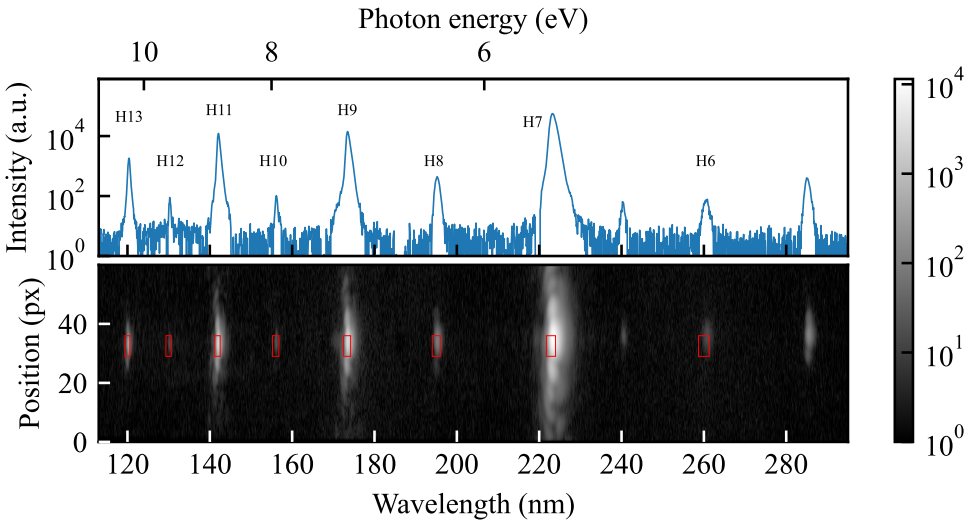

Fig. 4. Typical HHG spectrum generated in Al plasma, driven by the two-color fundamental field. The bottom panel shows the measured camera image of the HHG generated in the Al plasma. Red rectangles indicate integration areas for individual harmonic yields used in the data analysis for Fig. 7. The top panel shows the vertically integrated spectrum of the bottom panel, a.u. is arbitrary units. The ionization potential of Al is 5.98 eV.

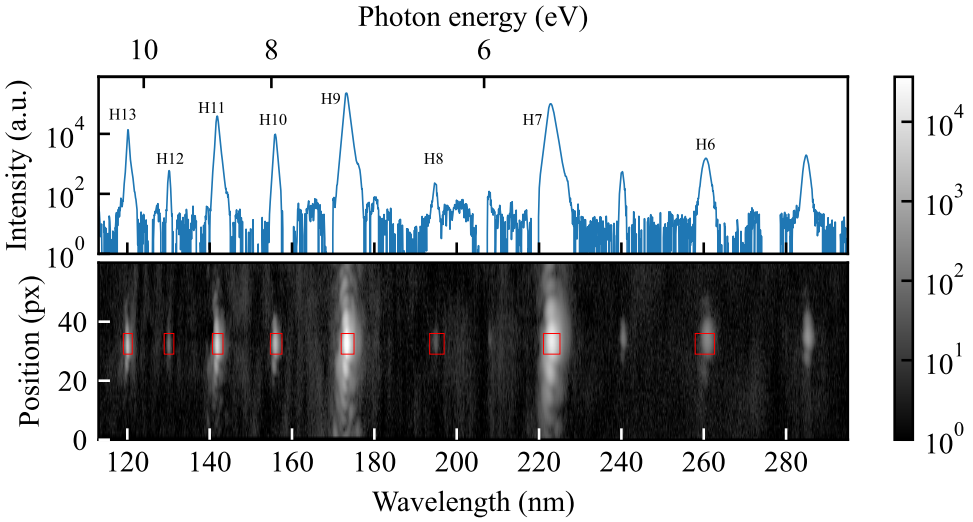

Fig. 5. Typical HHG spectrum generated in Sn plasma, driven by the two-color fundamental field. The bottom panel shows the measured camera image of the HHG generated in the Sn plasma. The red rectangles indicate integration areas for individual harmonic used in the data analysis for Fig. 8. The top panel shows the vertically integrated spectrum of the bottom panel, a.u. is arbitrary units. The ionization potential of Sn is 7.34 eV.

decreased. From these two figures, we observe a higher spectral intensity for nearly all the harmonics generated in a tin plasma, compared to the aluminium HHG spectrum. However, harmonics 7 and 8 are generated less efficiently in the tin plasma. Similar trends in the intensity of the odd harmonics have been observed before [32]. The near absence of harmonic 8 in the

Optics EXPRESS

tin HHG spectrum is surprising, especially since all other even harmonics up to order 12 are much brighter. From the present set of measurements it is not clear whether to attribute this to the single atom or ion response, or to differences in phase-matching conditions in the two LPPs. Further experiments involving controlled changes to the phase-matching conditions, e.g. by varying the interaction length, could provide further insights to this matter.

4.2. *Influence of second harmonic energy*

Figure 6(a) shows the generated HH spectra from aluminium plasmas upon increasing the strength of the second harmonic while keeping the fundamental beam energy constant. Note that the temporal overlap of fundamental and second harmonic pulses may be sub-optimal for the 0.5 μJ and 2 μJ second harmonic energies, as this has been optimized only for the 5 μJ second harmonic energy data. However, given the long duration of the fundamental pulses, this sub-optimal temporal overlap will not significantly alter the resulting HHG spectra. The absolute phase difference between the fundamental and its second harmonic have not been experimentally verified in this experiment as we are mainly interested in the behaviour for relative phase changes. The spectra in Fig. 6(a) are averaged over a range of wedge displacements corresponding to half an optical cycle of the second harmonic. Figure 6(b) shows the harmonic yield of the different even harmonics integrated over a 1% spectral bandwidth.

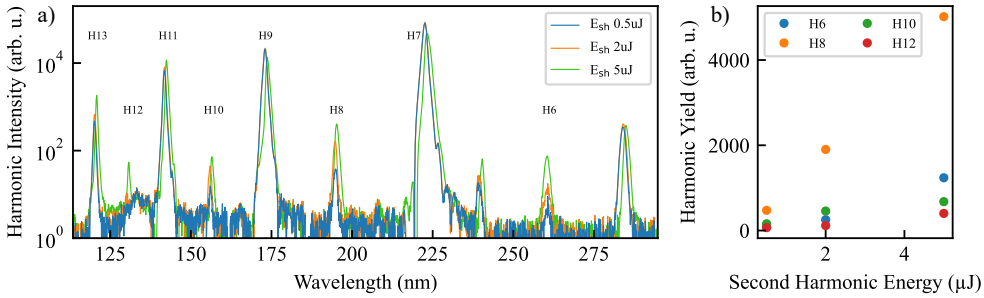

Fig. 6. a) High-harmonic spectra generated in Al plasma. Different curves correspond to different second-harmonic energies. b) Harmonic yields of even harmonics as a function of second-harmonic energy.

Figure 6(a) shows an increase in harmonic intensity for both odd and even harmonics when increasing the second harmonic energy from 0.5 μJ to 2 μJ. For the odd harmonics, this effect seems strongest for the highest-order harmonics detected. The signal increase for the even harmonics is most pronounced for central harmonics 8 and 10. Further increasing the second harmonic energy up to 5 μJ results in a lower intensity for odd harmonics 7 and 9, while all other harmonics are generated with a higher efficiency. This decrease might in part be attributed to slight changes in optical alignment between these two data sets, which have slightly decreased the generation efficiency of H7 and H9, while the increased presence of the second harmonic leads to stronger even harmonic signals due to the greater drive field asymmetry. Furthermore, the angle of the calcite plate has been tilted by 14° between the acquisition of the lowest two energies data set and the E_{SH} = 5 μJ data set to re-optimize even-order harmonic generation. For that reason, the direct comparison between these to data sets is not trivial. Nonetheless, the even-order harmonic yield grows linearly with increasing second-harmonic energy. Additionally, the stronger presence of the second harmonic favorably increased the phase-matching conditions to generate higher-order harmonics with higher efficiency. In contrast to the situation with parallel polarization, for which the ionization rate can increase strongly due to the second-harmonic field, our scheme with perpendicular polarization does not lead to significant changes in ionization

Optics EXPRESS

rate. This explains the limited effect of the SHG field on the yield of the odd harmonics and overall yield.

4.3. Phase-dependence of HHG in Al and Sn

Figure 7 shows the yield of all harmonics as a function of the relative phase between the fundamental and its second harmonic in aluminium. Figure 7(a) shows the individual harmonic yields integrated over the respective ROIs indicated in Fig. 4 on a logarithmic scale after the subtraction of background noise (explained in detail previously in [32]). Note that the absolute phase difference is not calibrated in these measurements. Instead, we measure harmonic signal fluctuations as a function of path length difference $\Delta\Lambda$. As a function of $\Delta\Lambda$, clear oscillatory behavior is observed for the even harmonics.

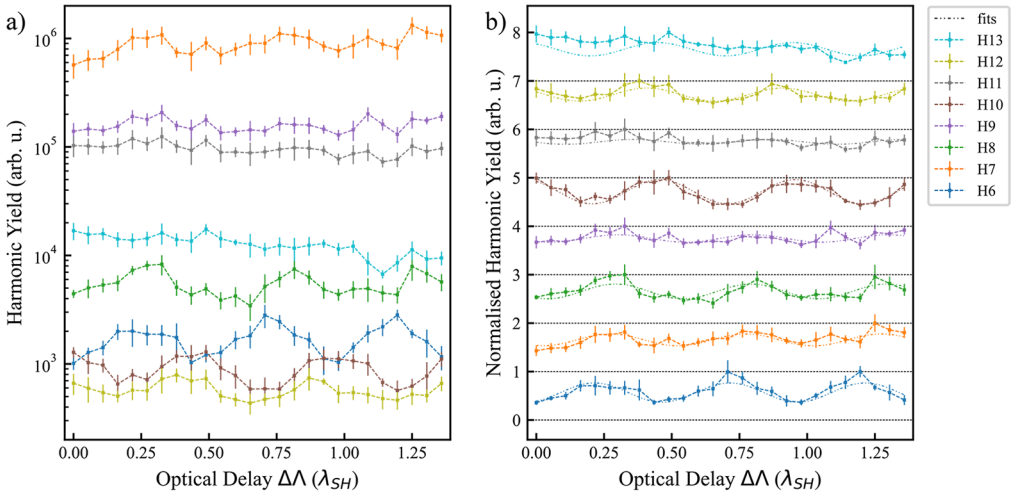

Fig. 7. Individual harmonic yields generated in the Al plasma as a function of relative phase between fundamental and second harmonic. a) Harmonic yields plotted on a logarithmic scale. b) Normalized harmonic yields plotted on a linear scale, and the traces are shifted vertically and sorted by increasing harmonic order for clarity.

To further visualize this oscillatory behavior, we have individually normalized these harmonic yields and plotted them with a vertical offset and sorted by increasing harmonic order (for clarity) in Fig. 7(b). The dash-dotted lines are fits to the model of Eq. (7), containing the expected oscillation period for the two-color fields. As the fits are in good agreement with the data, we can confidently state that these oscillations are actually the result of sub-cycle effects in the HHG process. The harmonics clearly oscillate with distinct phases, indicating differences in their electron trajectories. The extracted oscillation phases of the harmonics generated in Al are plotted in Fig. 9(a). Within the spectral range of these few harmonics, we observe a strong shift in oscillation phases of these harmonics. The harmonic oscillations shift their phases nearly linearly with emitted photon energy. A total phase difference of 0.94π is measured between lowest-order harmonic 6 and highest-order harmonic 13. However, harmonic 10, which shows the most clear oscillation signal, shows a jump in its oscillatory phase compared to the other harmonic orders. The measurements using an Sn target lead to similar results, as displayed in Fig. 8. As with the aluminium dataset, the left panel displays the harmonic yield for harmonic orders 6 to 13 with respect to the path length difference $\Delta\Lambda$, plotted on a logarithmic scale. For this dataset, the sub-cycle effects are not obviously visible in this raw data, as HHG intensity variations introduced by a slight curvature of the tin target obscures the oscillations of the harmonic intensities. For this reason, we have divided the results of Fig. 8(b) by the harmonic yield of harmonic order 11

Optics EXPRESS

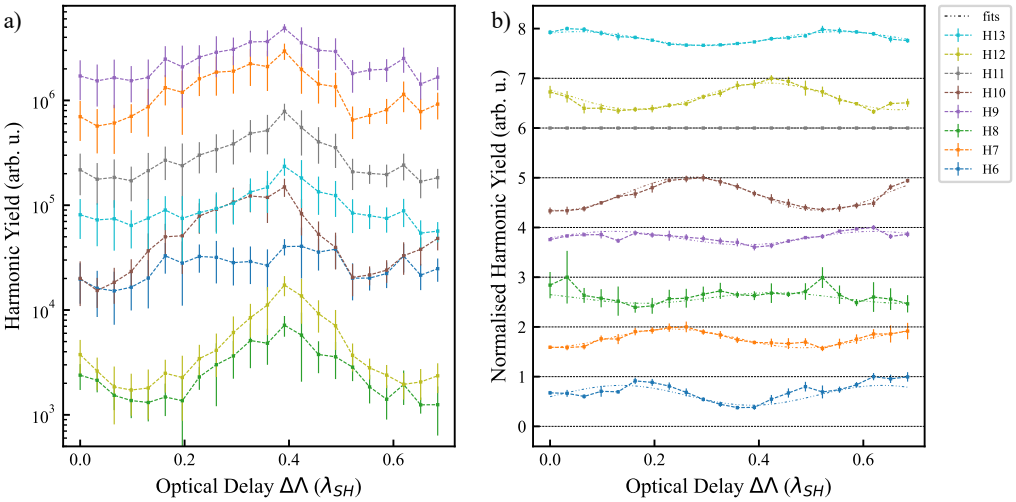

Fig. 8. Individual harmonic yields generated in the Sn plasma as a function of relative phase between fundamental and second harmonic. a) Harmonic yields plotted on a logarithmic scale. b) Normalized harmonic yields plotted on a linear scale. To remove sample-induced intensity variations from the measurement, every trace is divided by the yield of H11 after which the traces are individually normalized. Traces are shifted vertically and sorted by increasing harmonic order for clarity. For Al, only even-order harmonics are shown, as the odd-order harmonics did not show clear oscillations.

before the individual normalization. Here we have chosen harmonic order 11 to be our reference as its intensity is bright and its photon energy lies reasonably well above the first ionization potential of tin. Hence, we would not expect significant phase-dependent oscillations for this harmonic, making it a suitable reference signal to calibrate systematic intensity variations across the scan from other sources than the sub-cycle phase. Again, the harmonic yields are offset vertically for clarity. After this normalization, it becomes apparent that nearly every harmonic order is indeed oscillating with respect to the path length difference $\Delta\Lambda$. Only the oscillatory signal from harmonic 8 is less well defined due to a low signal-to-noise ratio, as is also apparent from Fig. 5. Again, the oscillation period matches with the expected path length variation of 390 nm, providing evidence of the presence of sub-cycle effects in the HHG process. Even more so compared to the aluminium case, harmonics generated in tin oscillate at very distinct phases. The fitted phases of the tin harmonic signals are plotted in Fig. 9(b). The fitted phase differences between adjacent harmonic orders vary from 1 radians up to multiple radians in this spectral range. Furthermore, no clear trend can be observed to describe the relation between the fitted phase and the harmonic order.

4.4. Pump-induced background fluorescence

In addition to the HHG radiation produced in aluminium and tin LPPs, we have also measured the pump-induced background fluorescence for both of these plasmas with the EUV spectrometer in the same spectral region as the measured harmonics. These fluorecence backgrounds have been measured in the absence of the fundamental beam and its second harmonic. The measured aluminium and tin emission spectra are plotted in Fig. 10(a) and (b), respectively. To assess possible overlap of absorption or emission lines with the HHG spectrum, blue markers indicate the wavelengths of the harmonics. The wavelengths corresponding to the ionization potentials of aluminium and tin have also been indicated within the plots. Finally, we have plotted cumulative spectra for various charge states of aluminium and tin in Figs. 10(a) and (b), obtained from the

Optics EXPRESS

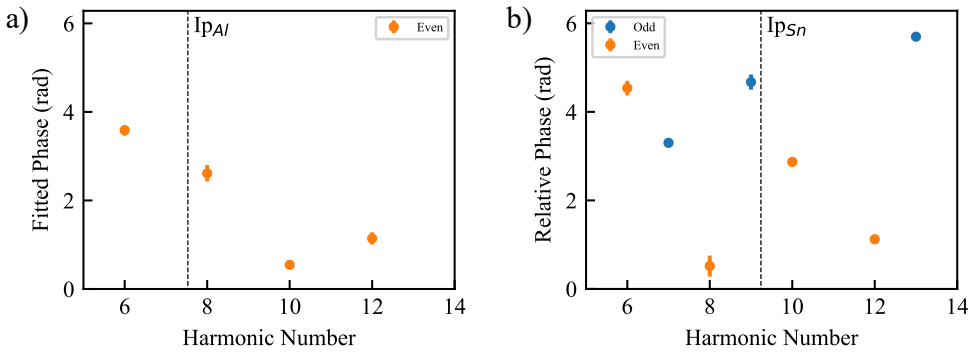

Fig. 9. Fitted phases for the harmonic orders generated in a) Al plasmas and b) Sn plasmas. The right panel misses a data point at harmonic order 11, as the harmonic yields for these data are taken relative to this harmonic, resulting in a constant signal strength. The ionization potentials of the elements are indicated by vertical dashed lines.

National Institute for Standards and Technology (NIST) Atomic Spectra Database [33]. Note that this database contains multiple sources with non-identical experimental conditions and normalization methods. For that reason, we have selected data that best match our recorded spectra, which are plotted as colored dashed lines.

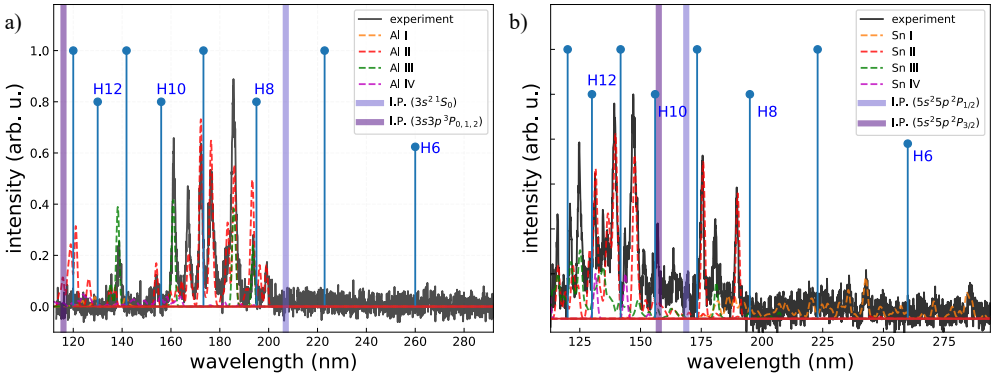

Fig. 10. Emission spectra of individual charge states overlaid onto experimental background plasma emission spectra of a) aluminium plasma, and b) tin plasma. Colored dashed lines represent cumulative EUV emission spectra obtained from the NIST database for line emission. Black solid lines represent experimentally measured background plasma emission. Blue pins correspond to wavelengths of high-order harmonics. Blue vertical stripes correspond to ionization potentials of Al and Sn.

For the aluminium LPP spectrum, mostly ion emission from Al II and Al III is observed. The cumulative NIST spectrum for Al II and Al III matches the emission profile quite well. However, some lines of the measured LPP emission are brighter or dimmer compared to the NIST spectrum. Especially the lines around 138 nm and 195 nm seem to lack intensity. This might be attributed to a changing charge-state composition in the plasma due to its expansion into the vacuum chamber [34], as the EUV camera integrates signals for all 157 pump pulses in a single exposure.

The composite NIST spectrum for the tin LPP also matches the experimentally obtained EUV spectrum quite well. This verifies the presence of Sn I, Sn II, Sn III and Sn IV species in the expanding plasma plume. Similar to the Al plasma spectrum, small discrepancies with the absolute intensities of individual lines are observed. Again, these differences between

Optics EXPRESS

experimental and NIST spectra might originate from different temperatures of the LPP due to its expansion in the vacuum chamber.

5. Discussion

From the obtained results we conclude that our HHG data contains effects due to subcycle dynamics in the different atomic species. To the best of our knowledge, this is the first observation of such dynamics in an LPP. In our experiments, we have limited the energy of the second harmonic to 1% of the fundamental, resulting in oscillating harmonic signals rather than completely switching harmonics on and off. In this configuration, we generate HHG spectra containing both odd and even harmonics. The even harmonic signal is roughly two orders of magnitude lower than the odd harmonic signal. Interestingly, for the HHG signal produced in Al, the even harmonic with the highest yield is harmonic 8, see Fig. 4, while this harmonic is actually the weakest in the case of HHG in tin, see Fig. 5. In the case of tin, all other harmonic orders appear stronger compared to the aluminium case.

Unlike the more commonly studied high-energy plateau regime where the strong field approximation holds [15,21,22,26,35,36], our present two-color HHG measurements in the low-order regime where the Coulomb potential cannot be neglected show different and interesting results between the two-color phase and the resulting HHG radiation. For HHG in aluminium, the even harmonics show oscillations as a function of path length difference $\Delta\Lambda$. This clearly indicates that indeed the dipole moment $\mathbf{d} = <\psi_g|\mathbf{r}|\psi_{el}>$ depends on the relative phase φ. From Fig. 9(a), it becomes clear that all even harmonics have a different relative phase ϕ_H, showing the dependency of the dipole moment $\mathbf{d}$ on harmonic frequency Ω. Interestingly, the odd-order harmonics do not seem to oscillate as a function of $\Delta\Lambda$. This might be due to a limited signal to noise ratio, or due to a smaller dependency of the dipole moment $\mathbf{d}$ on the relative phase φ, as our second harmonic acts as a small perturbation on the fundamental beam. From these limited points, the exact relation between these relative phases ϕ_H is still unclear, although there seems to be a decreasing trend for increasing harmonic number.

Clear oscillatory behavior is also observed for HHG in tin plasmas, although the signal to noise ratio for harmonic order 8 is too low for an accurate fit to Eq. (7). From the distinct phases observed for all other harmonics, we conclude that the normalization by harmonic 11 has not influenced the individual oscillations. Therefore, HHG in tin plasmas also shows a dependence of the dipole moment $\mathbf{d}$ on the relative phase φ, as well as the harmonic frequency Ω. In contrast to the Al case, for HHG in tin plasmas both odd and even orders oscillate as a function of $\Delta\Lambda$. Even more so compared to the aluminium data, the relative oscillation phase of individual harmonics ϕ_H for HHG in tin shows large differences for neighbouring harmonic orders, indicating a more pronounced effect of the Coulomb potential on the resulting HHG radiation.

Regarding any effects of resonant enhancement of specific harmonic-orders, harmonic-order 8 in the aluminium HHG spectrum is notably stronger than the other even harmonics, and its wavelength is close to an Al II emission line. However, harmonic order 10 is also close to an emission line from Al II, and is not particularly bright compared to harmonic order 12. Hence, we can not conclude a clear correlation between the ion emission spectrum and an enhanced HHG signal. For tin, harmonic order 10 in the HHG spectrum is stronger compared to the other even harmonic-orders while it lies close to the Sn $5s^2 5p^2 P_{3/2}$ ionization potential. Because Fig. 9(b) shows no clear trend for the oscillation phases of the harmonics, it is not possible to take the phase of harmonic-order 10 as an indicator for the presence of a resonant effect.

The results suggest that it would be beneficial to perform further experiments with shorter drive pulses, in order to extend the generated harmonic spectrum to shorter wavelengths. This would allow resonance-enhanced HHG for specific harmonics, like 47 nm in tin LPPs [10]. Combining such a measurement with a phase-controlled two-color drive laser would provide concrete data on the influence of a specific auto-ionizing state on the accumulated phase of the HHG trajectory.

Optics EXPRESS

Furthermore, a transition from a present, low-order regime where the Coulomb potential is important, to the better-known high-energy plateau regime might be found by examining a broad spectral range covering both low-order harmonics and high-order harmonics.

6. Conclusion

We have successfully generated high harmonics driven by a phase-controlled, two-color field with a fundamental wavelength at 1560 nm and its second harmonic at 780 nm in both aluminium and tin LPPs. Similar to the observed HHG spectral variation of odd harmonics generated in different media [32], the even harmonics generated in aluminium and tin also show clear differences in spectral intensity with identical driving fields. Upon increasing the second harmonic energy relative to the fundamental energy, the generation of even harmonics becomes more prominent as the second harmonic breaks the symmetry between the first and second half cycles of the fundamental wave.

Scanning the delay between the ω and 2ω fields gives rise to sub-cycle effects in the generation mechanism, resulting in the experimentally observed oscillations in the HHG signals. For aluminium, these oscillations are mostly observed for the even harmonic-orders. Tin HHG spectra show oscillating signals for both odd and even harmonic-orders. These oscillations have different amplitudes and phases for all generated harmonics. No clear relation between these phases and the harmonic frequency Ω can be extracted from these data, as neighboring harmonics show large jumps in oscillation phases. This suggests that the electron trajectories of the low-order harmonics observed in our experiment are not solely influenced by the electric field of the driving field, as is commonly assumed in the high-energy plateau regime where the strong field approximation holds. Instead, our measurements provide interesting results in the low-energy regime where the atomic Coulomb potential cannot be neglected in the electron acceleration phase of HHG, resulting in the strongly varying oscillation phases for individual harmonics.

Funding. Nederlandse Organisatie voor Wetenschappelijk Onderzoek.

Acknowledgments. The authors thank Nik Noest for technical support, and Dr. Aneta Stodolna, Dr. Tiago de Faria Pinto, Dr. Zeudi Mazzotta and Amelie Heinzerling for their contribution to the development of the setup. This work was carried out at ARCNL, a public-private partnership between the University of Amsterdam (UvA), Vrije Universiteit Amsterdam (VU), Rijksuniversiteit Groningen (RUG), the Dutch Research Council (NWO), and the semiconductor equipment manufacturer ASML.

Disclosures. The authors declare that they have no conflicts of interest.

Data availability. Data underlying the results presented in this paper are not publicly available at this time but may be obtained from the authors upon reasonable request.

References

1. A. McPherson, G. Gibson, H. Jara, *et al.*, "Studies of multiphoton production of vacuum-ultraviolet radiation in the rare gases," J. Opt. Soc. Am. B **4**(4), 595–601 (1987).
2. X. F. Li, A. L'Huillier, M. Ferray, *et al.*, "Multiple-harmonic generation in rare gases at high laser intensity," Phys. Rev. A **39**(11), 5751–5761 (1989).
3. P. A. Franken, A. E. Hill, C. W. Peters, *et al.*, "Generation of optical harmonics," Phys. Rev. Lett. **7**(4), 118–119 (1961).
4. G. H. C. New and J. F. Ward, "Optical third-harmonic generation in gases," Phys. Rev. Lett. **19**(10), 556–559 (1967).
5. P. Corkum, "Plasma perspective on strong field multiphoton ionization," Phys. Rev. Lett. **71**(13), 1994–1997 (1993).
6. M. Lewenstein, P. Balcou, M. Y. Ivanov, *et al.*, "Theory of high-harmonic generation by low-frequency laser fields," Phys. Rev. A **49**(3), 2117–2132 (1994).
7. P. M. Paul, E. S. Toma, P. Breger, *et al.*, "Observation of a train of attosecond pulses from high harmonic generation," Science **292**(5522), 1689–1692 (2001).
8. M. Suzuki, M. Baba, R. Ganeev, *et al.*, "Anomalous enhancement of a single high-order harmonic by using a laser-ablation tin plume at 47 nm," Opt. Lett. **31**(22), 3306–3308 (2006).
9. R. A. Ganeev, M. Suzuki, M. Baba, *et al.*, "Strong resonance enhancement of a single harmonic generated in the extreme ultraviolet range," Opt. Lett. **31**(11), 1699–1701 (2006).

Optics EXPRESS

10. M. A. Fareed, V. V. Strelkov, N. Thiré, *et al.*, "High-order harmonic generation from the dressed autoionizing states," Nat. Commun. **8**(1), 16061 (2017).
11. R. Ganeev, "High-order harmonic generation in laser plasma: Recent achievements," J. Phys. B: At., Mol. Opt. Phys. **40**(22), R213–R253 (2007).
12. R. Ganeev, M. Baba, M. Suzuki, *et al.*, "High-order harmonic generation from silver plasma," Phys. Lett. A **339**(1-2), 103–109 (2005).
13. R. A. Ganeev, M. Suzuki, M. Baba, *et al.*, "High-order harmonic generation from laser plasma produced by pulses of different duration," Phys. Rev. A **76**(2), 023805 (2007).
14. I. J. Kim, C. M. Kim, H. T. Kim, *et al.*, "Highly efficient high-harmonic generation in an orthogonally polarized two-color laser field," Phys. Rev. Lett. **94**(24), 243901 (2005).
15. N. Dudovich, O. Smirnova, J. Levesque, *et al.*, "Measuring and controlling the birth of attosecond XUV pulses," Nat. Phys. **2**(11), 781–786 (2006).
16. R. A. Ganeev, H. Singhal, P. A. Naik, *et al.*, "Systematic studies of two-color pump-induced high-order harmonic generation in plasma plumes," Phys. Rev. A **82**(5), 053831 (2010).
17. R. A. Ganeev, J. A. Chakera, P. A. Naik, *et al.*, "Resonance enhancement of single even harmonic of laser radiation in tin-containing plasma using intensity variation of two-color pump," J. Opt. Soc. Am. B **28**(5), 1055 (2011).
18. R. A. Ganeev, M. Suzuki, and H. Kuroda, "Quasi-phase-matching-induced enhancement of high-order harmonics during two-colour pump of multi-jet plasmas," J. Phys. B: At., Mol. Opt. Phys. **47**(10), 105401 (2014).
19. R. A. Ganeev, G. S. Boltaev, S. Y. Stremoukhov, *et al.*, "High-order harmonic generation during different overlaps of two-colored pulses in laser-produced plasmas and gases," Eur. Phys. J. D **74**(10), 199 (2020).
20. R. A. Ganeev, C. Hutchison, A. Zaïr, *et al.*, "Enhancement of high harmonics from plasmas using two-color pump and chirp variation of 1 kHz Ti:sapphire laser pulses," Opt. Express **20**(1), 90 (2012).
21. D. Shafir, H. Soifer, B. D. Bruner, *et al.*, "Resolving the time when an electron exits a tunnelling barrier," Nature **485**(7398), 343–346 (2012).
22. D. Shafir, Y. Mairesse, D. M. Villeneuve, *et al.*, "Atomic wavefunctions probed through strong-field light–matter interaction," Nat. Phys. **5**(6), 412–416 (2009).
23. L. Torlina and O. Smirnova, "Coulomb time delays in high harmonic generation," New J. Phys. **19**(2), 023012 (2017).
24. S. Yue, S. Xue, H. Du, *et al.*, "Revealing Coulomb time shifts in high-order harmonic generation by frequency-dependent streaking," Phys. Rev. A **105**(4), L041103 (2022).
25. S. Yue, J. Liu, S. Xue, *et al.*, "Observing the Coulomb shifts of ionization times in high-order harmonic generation," Phys. Rev. A **107**(6), 063102 (2023).
26. X. He, J. M. Dahlström, R. Rakowski, *et al.*, "Interference effects in two-color high-order harmonic generation," Phys. Rev. A **82**(3), 033410 (2010).
27. L. Young, D. A. Arms, E. M. Dufresne, *et al.*, "X-ray microprobe of orbital alignment in strong-field ionized atoms," Phys. Rev. Lett. **97**(8), 083601 (2006).
28. R. A. Meijer, A. S. Stodolna, K. S. E. Eikema, *et al.*, "High-energy Nd:YAG laser system with arbitrary sub-nanosecond pulse shaping capability," Opt. Lett. **42**(14), 2758–2761 (2017).
29. T. de Faria Pinto, J. Mathijssen, K. S. E. Eikema, *et al.*, "Optical parametric chirped pulse amplifier producing ultrashort 10.5 mj pulses at 1.55 um," Opt. Express **27**(21), 29829–29837 (2019).
30. S. D. C. Roscam Abbing, F. Campi, A. Zeltsi, *et al.*, "Divergence and efficiency optimization in polarization-controlled two-color high-harmonic generation," Sci. Rep. **11**(1), 24253 (2021).
31. I. H. Malitson, "Interspecimen comparison of the refractive index of fused silica," J. Opt. Soc. Am. **55**(10), 1205–1209 (1965).
32. J. Mathijssen, Z. Mazzotta, A. M. Heinzerling, *et al.*, "Material-specific high-order harmonic generation in laser-produced plasmas for varying plasma dynamics," Appl. Phys. B **129**(6), 91 (2023).
33. A. Kramida, Yu. Ralchenko, and J. Reader, and NIST ASD Team, NIST Atomic Spectra Database (ver. 5.10), [Online]. Available: https://physics.nist.gov/asd [2022, November 29]. National Institute of Standards and Technology, Gaithersburg, MD. (2022).
34. J. Scheers, R. Schupp, R. Meijer, *et al.*, "Time- and space-resolved optical stark spectroscopy in the afterglow of laser-produced tin-droplet plasma," Phys. Rev. E **102**(1), 013204 (2020).
35. G. Doumy, J. Wheeler, C. Roedig, *et al.*, "Attosecond synchronization of high-order harmonics from midinfrared drivers," Phys. Rev. Lett. **102**(9), 093002 (2009).
36. J. M. Dahlström, T. Fordell, E. Mansten, *et al.*, "Atomic and macroscopic measurements of attosecond pulse trains," Phys. Rev. A **80**(3), 033836 (2009).